LANGMUIR

pubs.acs.org/Langmuir Article

Enhancing Gas Solubility in Nanopores: A Combined Study Using Classical Density Functional Theory and Machine Learning

Chongzhi Qiao, Xiaochen Yu, Xianyu Song, Teng Zhao, Xiaofei Xu, Shuangliang Zhao,* and Keith E. Gubbins

Cite This: *Langmuir* 2020, 36, 8527−8536 Read Online

ACCESS | Metrics & More | Article Recommendations | Supporting Information

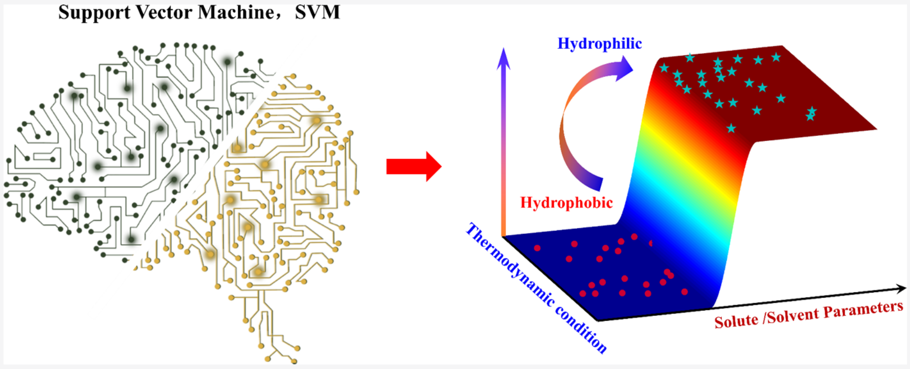

ABSTRACT: Geometrical confinement has a large impact on gas solubilities in nanoscale pores. This phenomenon is closely associated with heterogeneous catalysis, shale gas extraction, phase separation, etc. Whereas several experimental and theoretical studies have been conducted that provide meaningful insights into the over-solubility and under-solubility of different gases in confined solvents, the microscopic mechanism for regulating the gas solubility remains unclear. Here, we report a hybrid theoretical study for unraveling the regulation mechanism by combining classical density functional theory (CDFT) with machine learning (ML). Specifically, CDFT is employed to predict the solubility of argon in various solvents confined in nanopores of different types and pore widths, and these case studies then supply a valid training set to ML for further investigation. Finally, the dominant parameters that affect the gas solubility are identified, and a criterion is obtained to determine whether a confined gas−solvent system is enhance-beneficial or reduce-beneficial. Our findings provide theoretical guidance for predicting and regulating gas solubilities in nanopores. In addition, the hybrid method proposed in this work sets up a feasible platform for investigating complex interfacial systems with multiple controlling parameters.

1. INTRODUCTION

Solubility enhancement or suppression of gases in different solvents under confinement is receiving increasing interest, owing to its close association with molecular diffusion in porous materials,[1−3] mass transfer through membranes,[4] and surface catalytic reaction.[5−7] In recent decades, several experimental and theoretical works have been conducted to investigate gas solubilities in different confined solvents, and it has been reported that, in some cases, the gas solubility can be much enhanced in nanoconfinement; this phenomenon is often referred as to "over-solubility".[2,4,8−21] As a pioneering illustration, Peureux et al.[14] observed zero-order kinetics for the hydrogenation of nitrobenzene to aniline when molecular hydrogen gas and liquid nitrobenzene were confined in a γ-alumina membrane contactor, while first-order kinetics was observed in a conventional bulk slurry reactor. This difference in the reaction kinetics was interpreted to be due to an over-solubility of hydrogen gas in the confined nitrobenzene. Pera-Titus et al.[21] studied the solubility of hydrogen gas in confined $CHCl_3$, CCl_4, *n*-hexane, and ethanol, and they observed that the solubility of hydrogen gas could be enhanced by up to 15 times of its counterpart in the corresponding bulk solvents when the pore size was less than 15 nm. Budhathoki et al.[2] performed molecular dynamics simulations and observed an enhancement of CO_2 solubility in ionic liquids in carbon slit nanopores. This enhanced solubility led to increased perm-selectivities of CO_2 from a binary mixture of CO_2/CH_4. Furthermore, the enhanced solubilities of CO_2 in various confined solvents, including water,[15] propylene carbonate,[17]

Received: April 21, 2020
Revised: June 24, 2020
Published: July 6, 2020

and octamethycyclotetrasiloxane (OMCTS),[18] have also been reported. Despite these reports on over-solubility, a suppressed solubility known as under-solubility in confinement has also been observed. For example, under-solubility of ethanol[8] and sodium chloride[11] in confined water has been reported. These differences were attributed to the competition between two mechanisms:[13,22] the pore size effect and competitive adsorption mechanism. Also, we note that different studies have defined "solubility" differently, making comparisons of the solubility results from different studies less straightforward.[22]

However, a clear understanding of the factors that lead to under-solubility or over-solubility for a specified system remains to be resolved. In general, the gas solubility in confinement is related to system temperature, bulk pressure, pore width, wall−adsorbate interactions, and adsorbate−adsorbate interactions. It has been reported that the variation of adsorbate−wall interaction can greatly alter the physicochemical properties of a confined system.[23−27] For example, in our previous work,[23] we found that a decrease in adsorbate−wall interaction could enhance the contribution of adsorption pressure in nanopores and hence reduce the set pressure in pressure relief valves. Tao et al.[25] found that water permeability in a nanotube is reduced by decreasing the water−wall interaction. Furthermore, it has been reported that variation of the adsorbate−wall interaction affects the gas solubility.[9,28] Although the abovementioned experimental and theoretical studies provide important insights into the gas solubility in nanopores, the microscopic mechanism for manipulating the gas solubility remains unclear. The difficulty originates from the complex relation among the solubility and the multiple associated parameters.

To investigate this problem, in this work, we introduce a hybrid theoretical method by combining classical density functional theory (CDFT) and machine learning (ML). CDFT has been recognized as an efficient and accurate statistical mechanics method,[29] and it has been widely applied for investigating different interfacial systems, including gas adsorption in porous materials.[30,31] As demonstrated in our previous work,[22] CDFT can predict the gas solubility in confined solvents quantitatively. Moreover, the influence of the individual parameters such as pore width, system temperature, bulk pressure, and intermolecular potential parameters on gas solubility can be examined efficiently by means of CDFT. Nevertheless, CDFT calculations are often limited to case studies, and the system size that can be treated is typically on the nanoscale. As a result, it is difficult to give a comprehensive contour map of solubility over a wide range of multiple controlling parameters using CDFT alone. On the other hand, with the help of high-performance computing, ML has been accepted as a robust assistive tool in many research areas,[32−35] including different physicochemical systems.[34,36] Compared with CDFT calculations, ML has a generalization ability through which general criteria can be obtained based on a reliable training set. The training set is usually composed of the results from a few representative case studies, which can be conducted by using molecular simulations or CDFT. The combination of CDFT and ML can provide a feasible platform for unraveling the microscopic mechanisms of various complex systems with multiple controlling parameters. We expect that this combined study can give a universal phase diagram of the gas solubility in confined solvents on an experimentally achievable scale and thus guide the regulation of gas solubility in nanopores.

2. MODELING AND THEORY

2.1. Solubility in Confined Systems.

Following our previous work, the solubility of the solute gas, S_2, can be defined as[22]

$$S_2 = \frac{N_2}{N_1 + N_2} \times 100\% \tag{1}$$

where N_1 and N_2 represent the numbers of solvent and solute molecules, respectively. In a nanopore, N_i can be obtained by counting the molecular number in simulation realizations or by integrating the local density profile of the ith adsorbate, $\rho_i(\mathbf{r})$, over the entire confined space, i.e., $N_i = \int \rho_i(\mathbf{r})\mathrm{d}\mathbf{r}$. To obtain the density profiles of the solvent and solute in the nanopores, we consider a model system consisting of a mixture of two species (the adsorbates). We use the Lennard-Jones (12-6) model for the intermolecular adsorbate−adsorbate interactions and the Steele (10-4-3) potential[37] to describe the adsorbate−solid interaction. The Lennard-Jones potential gives a satisfactory description of the short-range repulsive interactions and the long-range attractive dispersion interactions and has been proven to give a good account of adsorption in many studies for molecules and substrates of the type considered here.[38−41] The Steele (10-4-3) potential is derived by summing the intermolecular pair potentials between a single adsorbate molecule and all atoms in the solid substrate. Comparisons of molecular simulations of adsorption using the Steele potential with those using a fully atomistic model of the solid show quantitative agreement, provided that the temperature is not very low.[42,43] For methane adsorbed in carbon pores, for example, the Steele potential gives very good results above about 80 K.[42]

$$u_{\mathrm{aw}}(z) = 2\pi\rho_{\mathrm{w}}\Delta_{\mathrm{w}}\varepsilon_{\mathrm{aw}}\sigma_{\mathrm{aw}}^2\left[\frac{2}{5}\left(\frac{\sigma_{\mathrm{aw}}}{z}\right)^{10} - \left(\frac{\sigma_{\mathrm{aw}}}{z}\right)^{4} - \left(\frac{\sigma_{\mathrm{aw}}^4}{3\Delta_{\mathrm{w}}(z + 0.61\Delta_{\mathrm{w}})^3}\right)\right] \tag{2}$$

where the subscripts a and w stand for the molecules of the absorbate and the wall, respectively. In eq 2, $\varepsilon_{\mathrm{aw}}$ and σ_{aw} are the energy and size parameters for the adsorbate−wall LJ interaction, respectively, and ρ_{w} is the atomic density of the wall. Here, different types of pore walls are considered with $\rho_{\mathrm{w}} = 114\ \mathrm{nm}^{-3}$ for graphite, $\rho_{\mathrm{w}} = 44.2\ \mathrm{nm}^{-3}$ for silica, and $\rho_{\mathrm{w}} = 25.4\ \mathrm{nm}^{-3}$ for mica. In eq 2, Δ_{w} is the interlayer spacing between layers of solid atoms, with $\Delta_{\mathrm{w}} = 0.335$ nm for graphite, $\Delta_{\mathrm{w}} = 0.220$ nm for silica, and $\Delta_{\mathrm{w}} = 0.287$ nm for mica.[44] The normal distance z in the above equation is defined as the separation between the mass center of an adsorbate molecule and the substrate surface, and the latter is specified as the plane through the centers of the substrate atoms in the outmost layer. While eq 2 gives the interaction energy of an adsorbate molecule with one wall, the total potential energy due to both walls is calculated by $u_{\mathrm{a,\,pore}}(z) = u_{\mathrm{aw}}(z) + u_{\mathrm{aw}}(H - z)$, where H is the pore width, defined as the separation between the planes through the surface atoms of the substrate on opposing walls of the slit pore (see Figure 1). Since argon is an inert gas and not subject to chemical reaction, argon is selected as the representative solute gas. All interaction parameters used in the present work are listed in Table 1. The interaction for unlike pairs is calculated using the Lorentz−Berthelot (LB) combination rules, i.e., $\varepsilon_{ij} = \sqrt{\varepsilon_{ii}\varepsilon_{jj}}$

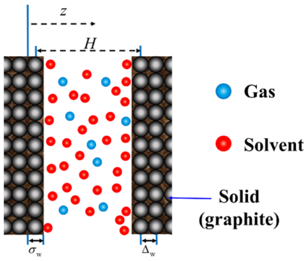

Figure 1. Schematic of the CDFT calculation system in this work.

Table 1. Lennard-Jones Pairwise Parameters of the Adsorbate and Adsorbent

species	ε/k_B (K)	σ (Å)
Ar[46]	119.8	3.40
CCl_4[47]	366.0	5.14
OMCTS[48]	351.4	7.70
$C_6H_5NO_2$[47]	425.0	5.14
C_6H_5Br[27]	351.2	5.38
graphite[49]	28.0	3.40
silica[47]	230.0	2.70
mica[44]	940.0	3.50

and $\sigma_{ij} = (\sigma_{ii} + \sigma_{jj})/2$. As shown in our previous work,[45] the porosity (pore size) and the fluid−solid interaction are of primary importance for determining the thermodynamics of confined fluids; the other characteristics, such as pore connectivity, pore size distribution, etc., play a less significant role. Hence, in this work, the porous material has been simplified as a simple slit pore model. The solvent and solution have been taken to be Lennard-Jones particles, and the Steele potential is used to describe the interaction between the solvent/solution and the solid. Based on these assumptions, we can significantly reduce the complexity of this system while maintaining crucial information.

2.2. Solubility Calculation by Classical Density Functional Theory. Classical density functional theory is formulated in the grand canonical ensemble (independent variables μ, V, T, where μ is chemical potential), for which the thermodynamic potential is the grand free energy, Ω. CDFT rests on a uniqueness theorem that states that it is possible to define a grand free energy functional, $\Omega[\rho(\mathbf{r})]$, that is a functional of the local density profile, $\rho(\mathbf{r})$, and that takes its minimum value, Ω, when the system reaches thermodynamic equilibrium. Given an expression for the grand free energy functional, it is possible to determine the density profile at equilibrium by using variational methods to minimize the free energy functional and from this the other equilibrium properties of the system.[29,50] Within the framework of CDFT, in the grand canonical ensemble, the grand potential functional of the adsorbate system is

$$\Omega[\rho_i(\mathbf{r})] = F^{\mathrm{id}}[\rho_i(\mathbf{r})] + F^{\mathrm{ex}}[\rho_i(\mathbf{r})] + \sum_i \int \rho_i(\mathbf{r})[V_i^{\mathrm{ext}}(\mathbf{r}) - \mu_i]\mathrm{d}\mathbf{r} \tag{3}$$

Here F^{id} and F^{ex} are the ideal gas and excess parts of the Helmholtz free energy, respectively. The term V_i^{ext} represents the external potential for the ith adsorbate component, which originates from the wall−adsorbate interaction, and μ_i is the bulk chemical potential, which is associated with the bulk density ρ_i^{b}. The ideal part of the Helmholtz free energy can be formulated analytically

$$F^{\mathrm{id}}[\rho_i(\mathbf{r})] = k_B T \sum_i \int \rho_i(\mathbf{r})[\ln \rho_i(\mathbf{r})\Lambda_i^{\,3} - 1]\mathrm{d}\mathbf{r} \tag{4}$$

Here, Λ_i is the de Broglie wavelength of the ith component, k_B is the Boltzmann constant, and T is the absolute temperature. In the present work, we adopt the first-order mean spherical approximation (FMSA) developed for LJ systems by Tang[51] to deal with the excess part of the Helmholtz free energy, $F^{\mathrm{ex}}[\rho_i(\mathbf{r})]$, in eq 3. In FMSA, F^{ex} consists of a repulsive part, $F^{\mathrm{ex}}_{\mathrm{rep}}[\rho_i(\mathbf{r})]$, and an attractive part, $F^{\mathrm{ex}}_{\mathrm{att}}[\rho_i(\mathbf{r})]$. The repulsive part accounts for the hard-sphere (HS) exclusion, while the effective HS diameter of each component can be estimated with the help of the Barker−Henderson formula.[52] The repulsive contribution is calculated by using the modified fundamental measure theory (MFMT).[53]

The attractive part, $F^{\mathrm{ex}}_{\mathrm{att}}$, is related to the bulk fluid at equilibrium and is given by a perturbation expansion truncated at the second order term

$$\beta F^{\mathrm{ex}}_{\mathrm{att}}[\rho_i(\mathbf{r})] = \beta F^{\mathrm{ex}}_{\mathrm{att}}(\rho_i^{\,\mathrm{b}}) + \sum_i \beta\mu_i^{\,\mathrm{att}} \int \Delta\rho_i(\mathbf{r})\mathrm{d}\mathbf{r} - \frac{1}{2}\sum_i\sum_j \int c_{ij}^{\mathrm{att}}(|\mathbf{r}_1 - \mathbf{r}_2|)\Delta\rho_i(\mathbf{r}_1)\Delta\rho_j(\mathbf{r}_2)\mathrm{d}\mathbf{r}_1\mathrm{d}\mathbf{r}_2 \tag{5}$$

where $\Delta\rho_i(\mathbf{r}) = \rho_i(\mathbf{r}) - \rho_i^{\mathrm{b}}$. Here, $\beta\mu_i^{\mathrm{att}}$ and $c_{ij}^{\mathrm{att}}(\mathbf{r})$ are the first- and the second-order differentials of $\beta F^{\mathrm{ex}}_{\mathrm{att}}[\rho_i(\mathbf{r})]$ with respect to the local density $\rho_i(\mathbf{r})$ at equilibrium, respectively, $\beta = 1/k_BT$, and the analytical expression of $c_{ij}^{\mathrm{att}}(\mathbf{r})$ can be found in the original work by Tang.[51]

In slab geometry, we have $\rho_i(\mathbf{r}) = \rho_i(z)$, with z being the direction perpendicular to the wall, and the external potential for the ith adsorbate, $V_i^{\mathrm{ext}}(z)$, is equivalent to $u_{\mathrm{a,\,pore}}(z)$. The minimization of the grand potential functional gives rise to the Euler−Lagrange equation, which finally reads

$$\rho_i(z) = \rho_i^{\,\mathrm{b}}\exp\left[-\beta V_i^{\mathrm{ext}}(z) + \sum_j \int c_{ij}^{\mathrm{att}}(|\mathbf{r}_1 - \mathbf{r}_2|)\Delta\rho_j(\mathbf{r}_2)\mathrm{d}\mathbf{r}_2 - \beta(\mu_i^{\,\mathrm{HS}}(z) - \mu_i^{\,\mathrm{b,HS}})\right] \tag{6}$$

Here, $\mu_i^{\mathrm{HS}}(z)$ is the local repulsive excess chemical potential and is calculated by using MFMT[53] with the help of the local density, $\rho_i(z)$; $\mu_i^{\mathrm{b,\,HS}}$ is the counterpart of $\mu_i^{\mathrm{HS}}(z)$ in the corresponding bulk system and is calculated from the Mansoori et al. equation of state (EOS).[54] The density profile in eq 6 can be obtained by using the steepest descent algorithm.[29]

For the CDFT calculation, the bulk densities of both solute and solvent are required. They can be determined by using the modified Benedict−Webb−Rubin (MBWR) EOS[55] at the given values of temperature and pressure. The calculation details of bulk density and bulk solubility at a given set of system temperatures and pressures are provided in the Supporting Information. The efficiency and accuracy of the above version of CDFT when applied to confined systems in

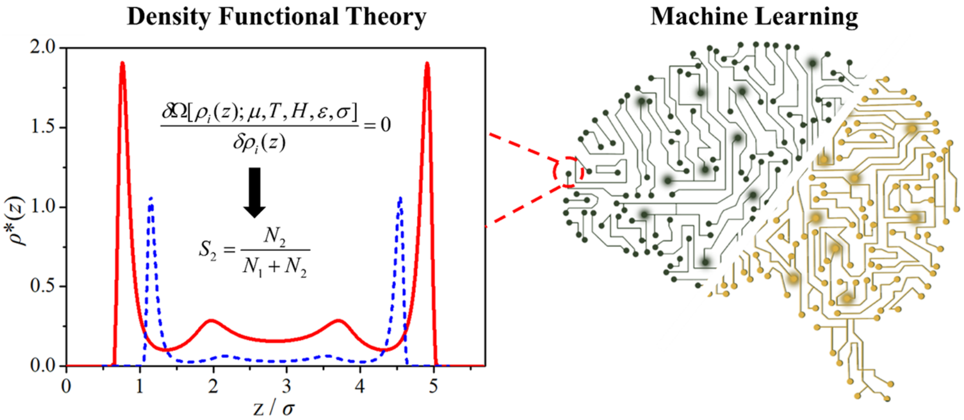

Figure 2. Schematic of the combination of CDFT and machine learning.

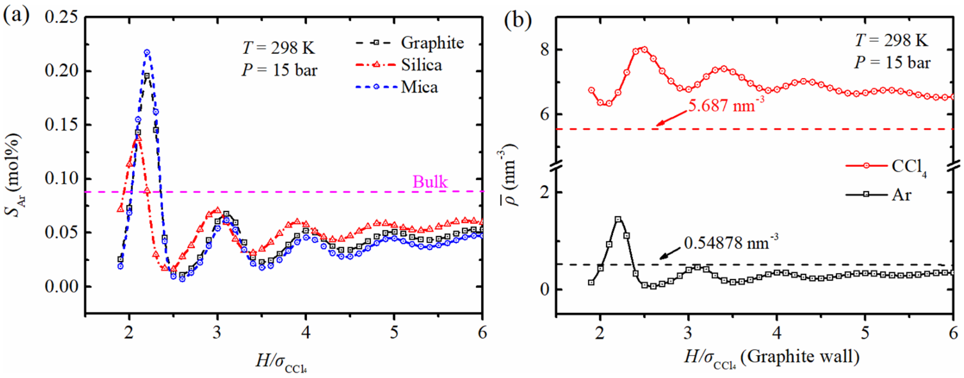

Figure 3. Argon uptake at 298 K and 15 bar bulk pressure in slit pores of varying pore width: (a) solubilities of argon in confined CCl_4 for three different walls and (b) density profiles for adsorbed argon (black points and line) and CCl_4 (red points and line) in carbon (graphite) pores. The horizontal dashed lines show the values of solubility and density for the bulk fluid under the same conditions of temperature and pressure.

slit-pore geometry have been validated in several previous works.[22−24,29−31]

2.3. Machine Learning with Input from CDFT Predictions. Machine learning is a useful approach for solving the classification and prediction of complex problems. As illustrated in Figure 2, the gas solubility under specific conditions (fixed pressure, temperature, solvent, solute, wall type, and pore size) can be predicted by using CDFT. Owing to the efficiency and accuracy of CDFT, many similar case studies can be carried out, and these supply individual logical points to ML. ML can then be used to find the hidden relation among these points. With the help of this relation, ML can thereafter predict the gas solubility for other cases or provide a general criterion to classify these points efficiently.

In general, ML algorithms can be divided into two types, supervised learning algorithms and semisupervised learning algorithms. Supervised learning algorithms build a mathematical model from a set of data that contains both the inputs and the desired outputs. The data is known as training data and consists of a set of training examples. Each training example has one or more inputs and a desired output, also known as a supervisory signal. Classification and regression are the two main branches of supervised algorithms. On the contrary, unsupervised learning algorithms take a set of data that contains only inputs and find structure in the data, like grouping or clustering of data points. The algorithms therefore learn from test data that has not been labeled, classified, or categorized.

In the present work, since we only considered the influence of four different parameters, i.e., σ_v/σ_s, $\varepsilon_v/\varepsilon_s$, P^* $(=P\sigma^3_{graphite}/\varepsilon_{graphite})$, and T^* $(=k_BT/\varepsilon_{graphite})$, based on some statistical heuristic methods,[56,57] we use 75 different systems as a training set and 25 different systems as a test set. Since, for smaller data sets, a supervised learning method known as support-vector machine (SVM)[58] always predicts a better performance than the conventional statistical method, SVM is used in the present work, and a detailed discussion about SVM is given below.

3. RESULTS AND DISCUSSION

3.1. Case Studies with CDFT: Argon Solubility in Nanopores. A confined solute−solvent system with argon as solute and CCl_4 as solvent is investigated at 298 K and 15 bar bulk pressure. The range of pore widths studied is from $1.9\sigma_{CCl_4}$ to $6.0\sigma_{CCl_4}$, with a discrete interval of $0.1\sigma_{CCl_4}$. Pore walls under consideration are graphite, silica, and mica. In Figure 3a, we show the CDFT predictions for the solubility of argon as a function of pore size with the presence of three different walls. Over-solubility is observed when H/σ_{CCl_4} is less than 2.5, while under-solubility is found when H/σ_{CCl_4} is larger than 2.5. Interestingly, argon solubility oscillates with pore width as pore size is increased. This oscillation phenomenon could also be interpreted in terms of the averaged concentrations of solvent and solute, $\bar{\rho}_i$, in the pore. The concentration of the ith adsorbate can be calculated by $\bar{\rho}_i = \frac{1}{H'}\int_0^H \rho_i(z)dz$, where $H' = H - \sigma_{aw}$ is the accessible pore

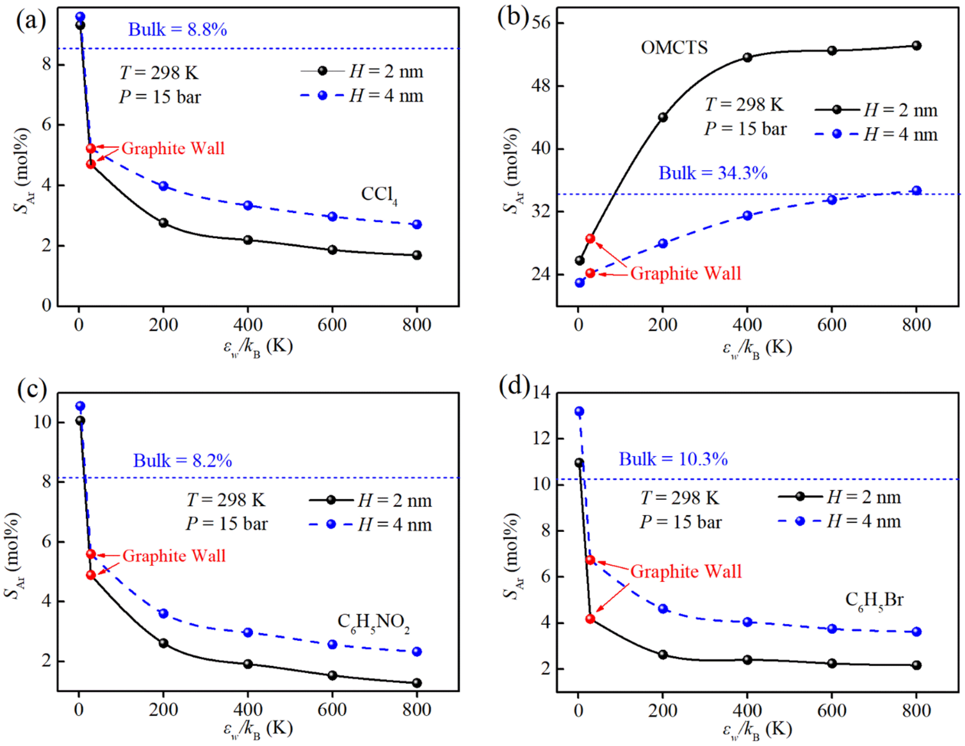

Figure 4. Argon solubilities in various solvents at 298 K and 15 bar bulk pressure in slit pores of various wall potentials with 2 (black solid lines) and 4 nm (blue dash lines) pore widths: (a) CCl_4, (b) OMCTS, (c) $C_6H_5NO_2$, (d) C_6H_5Br.

width.[22] As shown in Figure 3b, the averaged concentrations versus pore width also exhibit oscillations.

This oscillation in concentration can be explained by a combination of packing effects and competitive adsorption mechanism. The packing effect indicates that when the pore width is comparable to the size of the adsorbate molecule, the adsorbate forms a layer-by-layer structure in the pore due to the geometrical confinement. From Figure 3a, we can observe that for graphite, when the pore width is around 2.2σ, 3.1σ, 4.0σ, or 5.1σ, the argon solubility is higher than for nearby pore widths. This is because at these pore widths, the solvent molecules are prevented from forming dense and complete layers due to the steric constraints of the pore walls, and consequently, they are less packed. Thus, more space is available to accommodate solute molecules. At a width of 2.2σ, CCl_4 forms two loosely packed layers, leading to an enhanced adsorption of argon. The density of argon is much higher than that in the bulk system, as shown in Figure 3b. As a result, the solubility of argon in pores exhibits over-solubility.

The adsorption of argon and CCl_4 in each slit pore is a physical process according to Hu et al.[22] The molecule uptake of each component is mainly determined by the competitive adsorption mechanism. At a bulk pressure of 15 bar, the effect from the difference in the excess chemical potentials of the two components is relatively small, and in this circumstance, the wall−adsorbate interaction, i.e., the confinement effect, is the major factor in determining the density distribution. On the other hand, the wall−CCl_4 interaction is much more attractive than the wall−argon interaction, and thus, the adsorption of CCl_4 is more competitive, and this explains the enhancement of its concentration as shown in Figure 3b. On increasing the pore width, the confinement effect becomes less significant. As a result, the solubility and the density of both solute and solvent gradually recover to its bulk value as the pore width further increases.

It has been reported that the solubilities of N_2 and O_2 in water are enhanced by 5−10-fold when confined in hydrophobic pores[9] and the solubility of CH_4 in water is reduced in hydrophobic clay minerals.[28] Generally, when the wall potential well depth ε_w becomes larger, the interaction between the adsorbate and the solid surface becomes stronger, suggesting that the surface is more amphiphilic.[59,60] With the decrease of ε_w, the dispersion interaction becomes weaker, and the surface becomes amphiphobic. To further study the gas solubility in a confined solvent, we consider changes in the wall potential well depth, ε_w. A graphite wall (ε_w/k_B = 28 K) was chosen as a suitable benchmark for making comparisons. We chose wall potential well depths to be 3, 28, 200, 400, 600, and 800 K and set the pore width to be 2 and 4 nm, which are experimentally achievable sizes. All the other parameters and state conditions were kept the same as those of the graphite wall system considered above. The argon solubility, S_{Ar}, results are presented in Figure 4 for four different confined solvents (CCl_4, OMCTS, $C_6H_5NO_2$, C_6H_5Br). For the argon−CCl_4, argon−$C_6H_5NO_2$ and argon−C_6H_5Br systems, with increasing ε_w/k_B, the interaction between solute and solvent gradually increases, and we find that S_{Ar} decreases monotonically. Also, the S_{Ar} results indicate over-solubility when ε_w/k_B is less than about 5 K but display under-solubility for higher values of the wall energy parameter. By contrast, for the argon−OMCTS system, S_{Ar} increases with increasing ε_w/k_B, and we observe over-solubility when ε_w/k_B is larger than about 100 K in 2 nm slit pores and 700 K in 4 nm slit pores.

These phenomena indicate that for a confined gas−solvent system, we could regulate the gas solubility by modulating the wall−adsorbate interaction or the pore width. From an

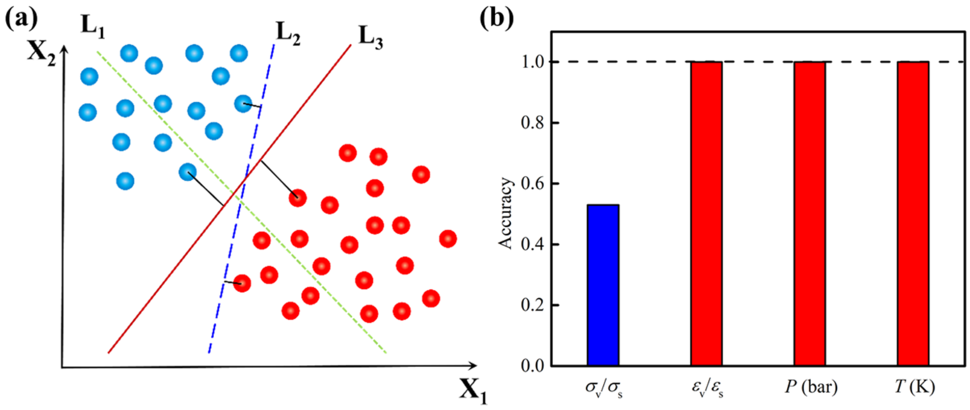

Figure 5. Schematic representations of (a) the principle of support-vector machine and (b) calculated accuracy.

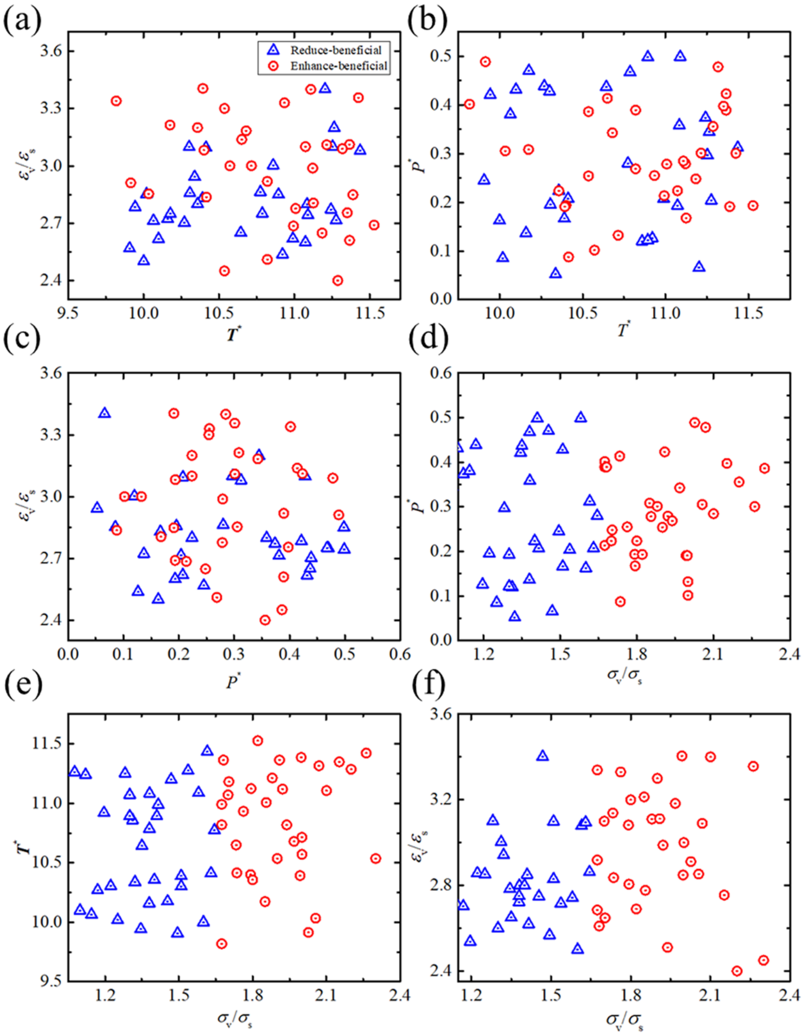

Figure 6. Scatter distribution of enhance-beneficial (red circles) and reduce-beneficial (blue triangles) systems for a pore of width 2.0 nm: (a) $T^* \sim \sigma_v/\sigma_s$, (b) $T \sim P^*$ ($P\sigma^3_{\text{graphite}}/\varepsilon_{\text{graphite}}$), (c) $P^* \sim \varepsilon_v/\varepsilon_s$, (d) $\sigma_v/\sigma_s \sim P^*$, (e) $\sigma_v/\sigma_s \sim\sim T^*$ ($k_BT/\varepsilon_{\text{graphite}}$), (f) $\sigma_v/\sigma_s \sim \varepsilon_v/\varepsilon_s$.

experimental perspective, we can change the adsorbent material, alter the pore wall surfaces, or change the pore width.

Furthermore, the abnormal gas solubility enhancement with increasing wall potential in the argon−OMCTS system suggests that there may be some deterministic factors to regulate the gas solubility in the confined space. If these factors are identified, we may be able to predict the solubility for other confined gas−solvent systems. For convenience, we define a system to be an enhance-beneficial system if the gas solubility is increased when enhancing the wall potential well depth. Otherwise, we refer to it as a reduce-beneficial system.

3.2. Incorporation with Machine Learning: Manipulation Mechanism.

Support-vector machine (SVM) is a supervised classifier, which has been proven to be highly effective in solving pattern recognition problems with a wide range.[61] The fundamental and core idea of SVM is to find a classification hyperplane to separate the data set into different classes. It is illustrated in Figure 5a, where L_1, L_2, and L_3 represent three different hyperplanes. It intuitively suggests that auxiliary line L_3 gives the best performance for classification, especially on the boundary or edge. This means that a good SVM classifier should be robust enough to tolerate the local "perturbation" and be of great generalization. In addition, SVM has low computational cost to solve nonlinear problems compared with other classifiers, such as decision-tree or logistic regression.

The general procedure for implementation of SVM can be divided into two steps. In the first place, the training data set is projected into higher dimensional space through the kernel function. Then, the machine finds a hyperplane that has the maximum margin to separate data vectors.

In this work, an initial SVM is constructed by considering four different parameters, i.e., σ_v/σ_s, $\varepsilon_v/\varepsilon_s$, P^* $(=P\sigma^3_{\text{graphite}}/\varepsilon_{\text{graphite}})$, and T^* $(=k_BT/\varepsilon_{\text{graphite}})$. Herein, the subscript v stands for solvent, and the subscript s represents solute species. We aim at using this SVM to classify whether a given confined solute−solvent system is an enhance-beneficial or a reduce-beneficial system. That is to say, the output category labels of SVM in this work are over-solubility and under-solubility.

First, we choose the data sets for sample training and testing. Argon is chosen as the solute, with LJ parameters σ_s = 3.4 Å and ε_s/k_B = 119.8 K. In this initial sample training and testing, we keep both the pore width, H = 2 nm, and the wall composition, graphite, fixed. The other parameters are considered with reasonable limits, which are $1.1 < \sigma_v/\sigma_s < 2.4$, $2.4 < \varepsilon_v/\varepsilon_s < 3.6$, $9.5 < T^* < 12$, and $0.05 < P^* < 0.51$. 100 different enhance-beneficial or reduce-beneficial confined solute−solvent systems are randomly generated with CDFT. 75 of them are selected as the training set, and the remaining 25 systems are the test set. We show that this trained SVM is good enough to give accurate predictions for the test set in what follows.

Second, by removing one of the four parameters, we obtain four new SVMs involving the remaining three parameters. Following training using these training sets, we can determine the accuracy of these four SVMs to describe the testing set. The accuracies of the four SVMs are presented in Figure 5b. The accuracy of the three SVMs when omitting $\varepsilon_v/\varepsilon_s$, P^*, and T^* still remains 100%. However, the accuracy of the SVM when omitting σ_v/σ_s is less than 60%. This result indicates that σ_v/σ_s is the dominant parameter in determining whether a specific confined solute−solvent system is enhance-beneficial or reduce-beneficial when H is fixed at 2.0 nm.

In Figure 6, by setting the four parameters σ_v/σ_s, $\varepsilon_v/\varepsilon_s$, P^*, and T^* as horizontal and vertical axes, respectively, we separate the confined solute−solvent systems into two categories. Red circles stand for enhance-beneficial systems, and blue triangles represent reduce-beneficial systems. From Figure 6a−c, one can see that when setting the three parameters $\varepsilon_v/\varepsilon_s$, P^*, and T^* as horizontal and vertical axes, respectively, the two different systems distribute randomly, indicating that we cannot separate these systems effectively by using these three parameters. However, if we set σ_v/σ_s as the horizontal axis and the remaining three parameters as the vertical axes, respectively, as illustrated in Figure 6d−f, one observes an obvious that if a system is an enhance-beneficial system or a reduce-beneficial system is only irrelevant with the ratio between solvent and solute particle sizes, σ_v/σ_s. This confirms the results from the ML analysis, namely, that the molecular size ratio between the solvent and solute σ_v/σ_s represents the dominant parameter to control whether a specific confined solute−solvent system is enhance-beneficial or reduce-beneficial.

To understand how this dominant parameter will affect the solubility, in Figure 7, we present the gas solubility ratio with respect to σ_v/σ_s and ε_w/k_B. This ratio is defined as the solubility in the confined solvent relative to that in the bulk solvent. If the gas solubility ratio is greater than 1, over-solubility occurs. Otherwise, we have under-solubility. Here, we take argon and OMCTS as the reference solute and solvent, respectively. Changing the parameter σ_v/σ_s is affected by varying the solvent molecule size, σ_v. The change in ε_w/k_B corresponds to altering the potential well depth of the pore wall. The black solid lines in both the lower-left corner and upper-right corner of Figure 7 represent the crossover from under- to over-solubility, i.e., the locus of points where the gas solubility in confined solvents equals that in the bulk solvent. In the lower-left corner in Figure 7, the confined solute−solvent systems are reduce-beneficial. Thereafter, the gas solubility gradually increases with the decrease of ε_w/k_B. Consequently, the gas solubility above the black line is suppressed, and that under the black line is enhanced. In the upper-right corner in Figure 7, the confined solute−solvent systems are enhance-beneficial. As a result, the gas solubility above the black line is enhanced, and the gas solubility under the black line is suppressed. It is noteworthy that when σ_v/σ_s is small, the confined solute−solvent system changes from over-solubility to under-solubility with the increase of ε_w/k_B. Conversely, when σ_v/σ_s is a large number, the situation is the opposite.

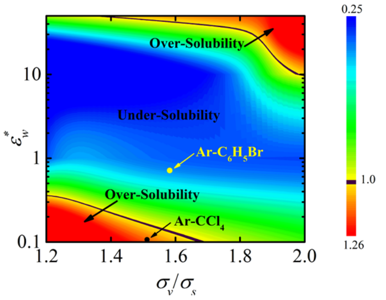

Figure 7. Evolution of the ratio of gas solubility in the slit pore and in the bulk phase with respect to σ_v/σ_s and $\varepsilon^*_w = \varepsilon_w/\varepsilon_{\text{graphite}}$ for a pore of width H = 2.0 nm. In these calculations, σ_w = 0.340 nm, the value for graphite. The three points here represent the real systems, i.e., argon−CCl_4, ε_w/k_B = 3 K (black point); argon−C_6H_5Br, ε_w/k_B = 20 K(yellow point).

In Figure 7, there are two over-solubility regions, the lower-left corner and the upper-right corner. To explain the difference between these over-solubility regions, we have considered the density distribution in these two regions. In the lower-left corner of Figure 7, this over-solubility is believed to occur because the higher ε_w/k_B will change the density distributions of both the large and small species. To verify this reasoning, the density distributions of a binary mixture confined in a slit pore with different ε_w/k_B and different σ_v/σ_s are shown in Figure 8. In Figure 8a, it is seen that when the sizes of two species are similar, increasing ε_w/k_B causes the

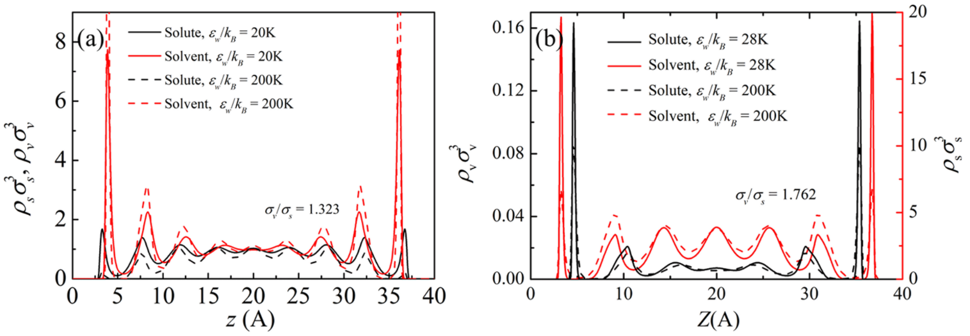

Figure 8. Density distribution of a binary mixture in a $H = 4.0$ nm slit pore: (a) The ratio of the diameter of the solute particle to that of the solvent particle, σ_v/σ_s, is 1.323. (b) The ratio of the diameter of the solute particle to that of the solvent particle, σ_v/σ_s, is 1.762.

density of the large species to increase and decreases the density of the small species. This can explain the mechanism of solubility enhancement of the lower-left corner in Figure 7. Also, this can explain the behavior of argon−solvent systems presented in Figure 4, but not the argon−OMCTS system. To explain the upper-right corner in Figure 7 and the behavior of the argon−OMCTS system, we also considered the density distribution when σ_v/σ_s is large, presented in Figure 8b. In Figure 8b, it is seen that when the sizes of two species are far different, increasing ε_w/k_B causes the density of both species to increase, and since the small solute particles are adsorbed in the void spaces between the big solvent particles, this leads to the density increase of small species that is faster than that of large species. This can explain the mechanism of solubility enhancement of the upper-right corner in Figure 7 and the behavior of the argon−OMCTS system.

4. CONCLUSIONS

The confinement effect on the gas solubility in nanopores has been investigated by combining CDFT with the ML method. Specifically, CDFT calculations provide the solubilities of argon gas in four confined solvents within nanopores of different pore widths and wall types. We demonstrate that the gas solubility can be altered by reducing the pore width or by varying the potential well depth of the pore wall. In total, 100 individual solute−solvent systems are examined, which supply a reliable training set to ML.

The combination of CDFT and ML can provide a powerful platform to unravel the microscopic mechanisms of various complex systems with multiple controlling parameters, in contrast to other works that are always limited to case-by-case studies. Two types of systems are defined according to the effect of the wall type on gas solubility. Enhance-beneficial systems are those for which the gas solubility increases on increasing the potential well depth of the pore wall. By contrast, in the reduce-beneficial systems, the gas solubility decreases on increasing the potential well depth. Both systems are distinguished with the help of this combined study. In addition, the combined study shows that the molecular size ratio between the solvent and solute, σ_v/σ_s, represents a dominant parameter. This gives a criterion for determining the over-solubility or under-solubility of gas in a confined solvent for a particular pore width of 2.0 nm.

This theoretical study gives mechanistic insights into the regulation of gas solubility in nanopores. Meanwhile, we demonstrate that the combination of CDFT and the ML method provides a feasible engineering tool to investigate the complex interfacial systems with multiple controlling parameters.

■ ASSOCIATED CONTENT

Supporting Information

The Supporting Information is available free of charge at https://pubs.acs.org/doi/10.1021/acs.langmuir.0c01160.

Calculation details of bulk density and bulk solubility (PDF)

■ AUTHOR INFORMATION

Corresponding Author

Shuangliang Zhao − *State Key Laboratory of Chemical Engineering and School of Chemical Engineering, East China University of Science and Technology, Shanghai 200237, China; Guangxi Key Laboratory of Petrochemical Resource Processing and Process Intensification Technology and School of Chemistry and Chemical Engineering, Guangxi University, Nanning 530004, China;* orcid.org/0000-0002-9547-4860; Email: szhao@ecust.edu.cn

Authors

Chongzhi Qiao − *State Key Laboratory of Chemical Engineering and School of Chemical Engineering, East China University of Science and Technology, Shanghai 200237, China*

Xiaochen Yu − *State Key Laboratory of Chemical Engineering and School of Chemical Engineering, East China University of Science and Technology, Shanghai 200237, China*

Xianyu Song − *State Key Laboratory of Chemical Engineering and School of Chemical Engineering, East China University of Science and Technology, Shanghai 200237, China;* orcid.org/0000-0003-2320-2599

Teng Zhao − *State Key Laboratory of Chemical Engineering and School of Chemical Engineering, East China University of Science and Technology, Shanghai 200237, China*

Xiaofei Xu − *State Key Laboratory of Chemical Engineering and School of Chemical Engineering, East China University of Science and Technology, Shanghai 200237, China;* orcid.org/0000-0003-2459-7748

Keith E. Gubbins − *Department of Chemical & Biomolecular Engineering, North Carolina State University, Raleigh, North Carolina 27695-7905, United States;* orcid.org/0000-0001-6760-5897

Complete contact information is available at: https://pubs.acs.org/10.1021/acs.langmuir.0c01160

Notes

■ ACKNOWLEDGMENTS

This work is supported by the National Natural Science Foundation of China (Nos. 91934302 and 21878078) and by the Shanghai Science and Technology Innovation Action Plan (18160743700) and by the 111 Project of China (grant no. B08021). K.E.G. thanks the U.S. National Science Foundation for support of this work under grant no. CBET-1603851.

■ REFERENCES

(1) Hu, H.; Zhang, J.; Guo, S.; Chen, G. Extraction of Huadian Oil Shale with Water in Sub- and Supercritical States. *Fuel* **1999**, *78*, 645−651.

(2) Budhathoki, S.; Shah, J. K.; Maginn, E. J. Molecular Simulation Study of the Performance of Supported Ionic Liquid Phase Materials for the Separation of Carbon Dioxide from Methane and Hydrogen. *Ind. Eng. Chem. Res.* **2017**, *56*, 6775−6784.

(3) Jin, Z.; Firoozabadi, A. Thermodynamic Modeling of Phase Behavior in Shale Media. *SPE J.* **2016**, *21*, 190−207.

(4) Pera-Titus, M.; Miachon, S.; Dalmon, J.-A. Increased Gas Solubility in Nanoliquids: Improved Performance in Interfacial Catalytic Membrane Contactors. *AIChE J.* **2009**, *55*, 434−441.

(5) Liu, C.-C.; Mou, C.-Y.; Yu, S. S. F.; Chan, S. I. Heterogeneous Formulation of the Tricopper Complex for Efficient Catalytic Conversion of Methane into Methanol at Ambient Temperature and Pressure. *Energy Environ. Sci.* **2016**, *9*, 1361−1374.

(6) Ostrovsky, V. E. Combined Use of Calorimetric and Adsorption Kinetic Methods for the Study of the Mechanisms of Catalytic Processes. *J. Therm. Anal.* **1978**, *14*, 27−43.

(7) O'Brien, M.; Taylor, N.; Polyzos, A.; Baxendale, I. R.; Ley, S. V. Hydrogenation in Flow: Homogeneous and Heterogeneous Catalysis Using Teflon AF-2400 to Effect Gas−Liquid Contact at Elevated Pressure. *Chem. Sci.* **2011**, *2*, 1250.

(8) Ratajska-Gadomska, B.; Gadomski, W. Influence of Confinement on Solvation of Ethanol in Water Studied by Raman Spectroscopy. *J. Chem. Phys.* **2010**, *133*, 234505.

(9) Luzar, A.; Bratko, D. Gas Solubility in Hydrophobic Confinement. *J. Phys. Chem. B* **2005**, *109*, 22545−22552.

(10) Bratko, D.; Luzar, A. Attractive Surface Force in the Presence of Dissolved Gas: A Molecular Approach. *Langmuir* **2008**, *24*, 1247−1253.

(11) Malani, A.; Ayappa, K. G.; Murad, S. Effect of Confinement on the Hydration and Solubility of NaCl in Water. *Chem. Phys. Lett.* **2006**, *431*, 88−93.

(12) Ho, L. N.; Schuurman, Y.; Farrusseng, D.; Coasne, B. Solubility of Gases in Water Confined in Nanoporous Materials: ZSM-5, MCM-41, and MIL-100. *J. Phys. Chem. C* **2015**, *119*, 21547−21554.

(13) Ho, L. N.; Clauzier, S.; Schuurman, Y.; Farrusseng, D.; Coasne, B. Gas Uptake in Solvents Confined in Mesopores: Adsorption versus Enhanced Solubility. *J. Phys. Chem. Lett.* **2013**, *4*, 2274−2278.

(14) Peureux, J.; Torres, M.; Mozzanega, H.; Giroir-Fendler, A.; Dalmon, J.-A. Nitrobenzene Liquid-Phase Hydrogenation in a Membrane Reactor. *Catal. Today* **1995**, *25*, 409−415.

(15) Soubeyrand-Lenoir, E.; Vagner, C.; Yoon, J. W.; Bazin, P.; Ragon, F.; Hwang, Y. K.; Serre, C.; Chang, J.-S.; Llewellyn, P. L. How Water Fosters a Remarkable 5-Fold Increase in Low-Pressure CO 2 Uptake within Mesoporous MIL-100(Fe). *J. Am. Chem. Soc.* **2012**, *134*, 10174−10181.

(16) Qiao, Y.; Cao, G.; Chen, X. Effects of Gas Molecules on Nanofluidic Behaviors. *J. Am. Chem. Soc.* **2007**, *129*, 2355−2359.

(17) Ho, N. L.; Porcheron, F.; Pellenq, R. J. M. Experimental and Molecular Simulation Investigation of Enhanced CO_2 Solubility in Hybrid Adsorbents. *Langmuir* **2010**, *26*, 13287−13296.

(18) Ho, L. N.; Perez Pellitero, J.; Porcheron, F.; Pellenq, R. J. M. Enhanced CO_2 Solubility in Hybrid MCM-41: Molecular Simulations and Experiments. *Langmuir* **2011**, *27*, 8187−8197.

(19) Clauzier, S.; Ho, L. N.; Pera-Titus, M.; Coasne, B.; Farrusseng, D. Enhanced H_2 Uptake in Solvents Confined in Mesoporous Metal−Organic Framework. *J. Am. Chem. Soc.* **2012**, *134*, 17369−17371.

(20) Rakotovao, V.; Ammar, R.; Miachon, S.; Pera-Titus, M. Influence of the Mesoconfining Solid on Gas Oversolubility in Nanoliquids. *Chem. Phys. Lett.* **2010**, *485*, 299−303.

(21) Pera-Titus, M.; El-Chahal, R.; Rakotovao, V.; Daniel, C.; Miachon, S.; Dalmon, J.-A. Direct Volumetric Measurement of Gas Oversolubility in Nanoliquids: Beyond Henry's Law. *ChemPhysChem* **2009**, *10*, 2082−2089.

(22) Hu, Y.; Huang, L.; Zhao, S.; Liu, H.; Gubbins, K. E. Effect of Confinement in Nano-Porous Materials on the Solubility of a Supercritical Gas. *Mol. Phys.* **2016**, *114*, 3294−3306.

(23) Yu, X.; Zhang, J.; Zhao, S.; Yu, X.; Liu, H. An Investigation into the Effect of Gas Adsorption on Safety Valve Set Pressure Variations. *Chem. Eng. Sci.* **2018**, *188*, 170−178.

(24) Yu, X.; Tang, W.; Zhao, T.; Jin, Z.; Zhao, S.; Liu, H. Confinement Effect on Molecular Conformation of Alkanes in Water-Filled Cavitands: A Combined Quantum/Classical Density Functional Theory Study. *Langmuir* **2018**, *34*, 13491−13496.

(25) Tao, J.; Song, X.; Zhao, T.; Zhao, S.; Liu, H. Confinement Effect on Water Transport in CNT Membranes. *Chem. Eng. Sci.* **2018**, *192*, 1252−1259.

(26) An, R.; Huang, L.; Long, Y.; Kalanyan, B.; Lu, X.; Gubbins, K. E. Liquid−Solid Nanofriction and Interfacial Wetting. *Langmuir* **2016**, *32*, 743−750.

(27) Radhakrishnan, R.; Gubbins, K. E.; Sliwinska-Bartkowiak, M. Effect of the Fluid-Wall Interaction on Freezing of Confined Fluids: Toward the Development of a Global Phase Diagram. *J. Chem. Phys.* **2000**, *112*, 11048−11057.

(28) Gadikota, G.; Dazas, B.; Rother, G.; Cheshire, M. C.; Bourg, I. C. Hydrophobic Solvation of Gases (CO_2, CH_4, H_2, Noble Gases) in Clay Interlayer Nanopores. *J. Phys. Chem. C* **2017**, *121*, 26539−26550.

(29) Zhao, S.; Liu, Y.; Chen, X.; Lu, Y.; Liu, H.; Hu, Y. Unified Framework of Multiscale Density Functional Theories and Its Recent Applications. In *Advances in Chemical Engineering*; Elsevier, 2015; Vol. *47*, pp 1−83.

(30) Liu, Y.; Zhao, S.; Liu, H.; Hu, Y. High-Throughput and Comprehensive Prediction of H_2 Adsorption in Metal-Organic Frameworks under Various Conditions. *AIChE J.* **2015**, *61*, 2951−2957.

(31) Liu, Y.; Liu, H.; Hu, Y.; Jiang, J. Density Functional Theory for Adsorption of Gas Mixtures in Metal−Organic Frameworks. *J. Phys. Chem. B* **2010**, *114*, 2820−2827.

(32) Holloway, P.; Kudenko, D.; Bell, J. R. Dynamic Selection of Environmental Variables to Improve the Prediction of Aphid Phenology: A Machine Learning Approach. *Ecol. Indic.* **2018**, *88*, 512−521.

(33) Ma, X.; Li, Z.; Achenie, L. E. K.; Xin, H. Machine-Learning-Augmented Chemisorption Model for CO 2 Electroreduction Catalyst Screening. *J. Phys. Chem. Lett.* **2015**, *6*, 3528−3533.

(34) Rupp, M.; Ramakrishnan, R.; von Lilienfeld, O. A. Machine Learning for Quantum Mechanical Properties of Atoms in Molecules. *J. Phys. Chem. Lett.* **2015**, *6*, 3309−3313.

(35) Saito, Y.; Oikawa, M.; Nakazawa, H.; Niide, T.; Kameda, T.; Tsuda, K.; Umetsu, M. Machine-Learning-Guided Mutagenesis for Directed Evolution of Fluorescent Proteins. *ACS Synth. Biol.* **2018**, *7*, 2014−2022.

(36) Novikov, I. S.; Suleimanov, Y. V.; Shapeev, A. V. Automated Calculation of Thermal Rate Coefficients Using Ring Polymer Molecular Dynamics and Machine-Learning Interatomic Potentials with Active Learning. *Phys. Chem. Chem. Phys.* **2018**, *20*, 29503−29512.

(37) Steele, W. A. *The Interaction of Gases with Solid Surfaces*; Pergamon Press: Oxford, 1974.

(38) Gubbins, K. E.; Liu, Y.-C.; Moore, J. D.; Palmer, J. C. The Role of Molecular Modeling in Confined Systems: Impact and Prospects. *Phys. Chem. Chem. Phys.* **2011**, *13*, 58−85.

(39) Palmer, J. C.; Moore, J. D.; Roussel, T. J.; Brennan, J. K.; Gubbins, K. E. Adsorptive Behavior of CO2, CH4 and Their Mixtures in Carbon Nanospace: A Molecular Simulation Study. *Phys. Chem. Chem. Phys.* **2011**, *13*, 3985.

(40) Palmer, J. C.; Moore, J. D.; Brennan, J. K.; Gubbins, K. E. Simulating Local Adsorption Isotherms in Structurally Complex Porous Materials: A Direct Assessment of the Slit Pore Model. *J. Phys. Chem. Lett.* **2011**, *2*, 165−169.

(41) Gubbins, K. E.; Long, Y.; Śliwinska-Bartkowiak, M. Thermodynamics of Confined Nano-Phases. *J. Chem. Thermodyn.* **2014**, *74*, 169−183.

(42) Jiang, S.; Rhykerd, C. L.; Gubbins, K. E. Layering, Freezing Transitions, Capillary Condensation and Diffusion of Methane in Slit Carbon Pores. *Mol. Phys.* **1993**, *79*, 373−391.

(43) Miyahara, M.; Gubbins, K. E. Freezing/Melting Phenomena for Lennard-Jones Methane in Slit Pores: A Monte Carlo Study. *J. Chem. Phys.* **1997**, *106*, 2865−2880.

(44) Cui, S. T.; McCabe, C.; Cummings, P. T.; Cochran, H. D. Molecular Dynamics Study of the Nano-Rheology of n-Dodecane Confined between Planar Surfaces. *J. Chem. Phys.* **2003**, *118*, 8941−8944.

(45) Qiao, C. Z.; Zhao, S. L.; Liu, H. L.; Dong, W. Connect the Thermodynamics of Bulk and Confined Fluids: Confinement-Adsorption Scaling. *Langmuir* **2019**, *35*, 3840−3847.

(46) Hirsehfelder, J. O.; Curtiss, C. F.; Bird, R. B. *Molecular Theory of Gases and Liquids*. Wiley:New York 1954.

(47) Radhakrishnan, R.; Gubbins, K. E.; Sliwinska-Bartkowiak, M. Global Phase Diagrams for Freezing in Porous Media. *J. Chem. Phys.* **2002**, *116*, 1147−1155.

(48) Ayappa, K. G.; Mishra, R. K. Freezing of Fluids Confined between Mica Surfaces. *J. Phys. Chem. B* **2007**, *111*, 14299−14310.

(49) Steele, W. A. The Physical Interaction of Gases with Crystalline Solids: I. Gas-Solid Energies and Properties of Isolated Adsorbed Atoms. *Surf. Sci.* **1973**, *36*, 317−352.

(50) Evans, R. The Nature of the Liquid-Vapour Interface and Other Topics in the Statistical Mechanics of Non-Uniform, Classical Fluids. *Adv. Phys.* **1979**, *28*, 143−200.

(51) Tang, Y. First-Order Mean Spherical Approximation for Inhomogeneous Fluids. *J. Chem. Phys.* **2004**, *121*, 10605−10610.

(52) Barker, J. A.; Henderson, D. Perturbation Theory and Equation of State for Fluids. II. A Successful Theory of Liquids. *J. Chem. Phys.* **1967**, *47*, 4714−4721.

(53) Yu, Y.-X.; Wu, J.; Xin, Y.-X.; Gao, G.-H. Structures and Correlation Functions of Multicomponent and Polydisperse Hard-Sphere Mixtures from a Density Functional Theory. *J. Chem. Phys.* **2004**, *121*, 1535−1541.

(54) Mansoori, G. A.; Carnahan, N. F.; Starling, K. E.; Leland, T. W., Jr. Equilibrium Thermodynamic Properties of the Mixture of Hard Spheres. *J. Chem. Phys.* **1971**, *54*, 1523−1525.

(55) Johnson, J. K.; Zollweg, J. A.; Gubbins, K. E. The Lennard-Jones Equation of State Revisited. *Mol. Phys.* **1993**, *78*, 591−618.

(56) Raudys, S. J.; Jain, A. K. Small Sample Size Effects in Statistical Pattern Recognition: Recommendations for Practitioners. *IEEE Trans. Pattern Anal. Mach. Intell.* **1991**, *13*, 252−264.

(57) Beleites, C.; Neugebauer, U.; Bocklitz, T.; Krafft, C.; Popp, J. Sample Size Planning for Classification Models. *Anal. Chim. Acta* **2013**, *760*, 25−33.

(58) Hua, S.; Sun, Z. A Novel Method of Protein Secondary Structure Prediction with High Segment Overlap Measure: Support Vector Machine Approach. *J. Mol. Biol.* **2001**, *308*, 397−407.

(59) Śliwińska-Bartkowiak, M.; Sterczyńska, A.; Long, Y.; Gubbins, K. E. Influence of Microroughness on the Wetting Properties of Nano-Porous Silica Matrices. *Mol. Phys.* **2014**, *112*, 2365−2371.

(60) Ingebrigtsen, T.; Toxvaerd, S. Contact Angles of Lennard-Jones Liquids and Droplets on Planar Surfaces. *J. Phys. Chem. C* **2007**, *111*, 8518−8523.

(61) Chauhan, V. K.; Dahiya, K.; Sharma, A. Problem Formulations and Solvers in Linear SVM: A Review. *Artif. Intell. Rev.* **2019**, *52*, 803−855.